

CERTIFYING NEURAL NETWORK AUDIO CLASSIFIERS

Anonymous authors

Paper under double-blind review

ABSTRACT

We present the first end-to-end verifier of audio classifiers. Compared to existing methods, our approach enables analysis of both, the entire audio processing stage as well as recurrent neural network architectures (e.g., LSTM). The audio processing is verified using novel convex relaxations tailored to feature extraction operations used in audio (e.g., Fast Fourier Transform) while recurrent architectures are certified via a novel binary relaxation for the recurrent unit update. We show the verifier scales to large networks while computing significantly tighter bounds than existing methods for common audio classification benchmarks: on the challenging Google Speech Commands dataset we certify 95% more inputs than the interval approximation (only prior scalable method), for a perturbation of -90dB.

1 INTRODUCTION

Recent advances in deep learning have enabled replacement of traditional voice recognition systems with a single neural network trained from data (Graves et al., 2013; Hannun et al., 2014; Amodei et al., 2016). Wide adoption of these networks in consumer devices poses a threat to their safety when exposed to a malicious adversary. Indeed, it was recently shown that an adversary can inject noise unrecognizable to a human and force the network to misclassify (Szegedy et al., 2013; Goodfellow et al., 2014; Zhang et al., 2017; Carlini & Wagner, 2018; Carlini et al., 2016; Qin et al., 2019; Neehara et al., 2019; Yang et al., 2019; Esmailpour et al., 2019), exposing a serious security flaw.

Ideally, when deploying an automated speech recognition system we would like to guarantee that the system is robust against noise injected by an adversary. There has been substantial recent work on certifying robustness of computer vision models (Katz et al., 2017; Ehlers, 2017; Bunel et al., 2018; Ruan et al., 2018; Tjeng et al., 2019; Anderson et al., 2018; Wong et al., 2018; Dvijotham et al., 2018; Raghunathan et al., 2018; Dvijotham et al., 2019; Weng et al., 2018; Zhang et al., 2018; Salman et al., 2019; Gehr et al., 2018; Singh et al., 2018; 2019a; Wang et al., 2018; Singh et al., 2019b). However, the audio domain poses unique challenges not addressed by prior certification work for vision.

Differences between audio and vision models Concretely, while an input to a vision model is a raw image, audio models typically come with a complex preprocessing stage (that involves non-trivial non-linear operations such as logarithm) which extracts relevant features from the signal. Additionally, audio systems typically use recurrent architectures (Chiu et al., 2017) which computer vision verifiers do not handle as they focus on fully-connected, convolutional and residual architectures.

This work We address both of these challenges and propose an end-to-end verification method for neural network based audio classifiers and an implementation of this method in a system called DAC (Deep Audio Certifier). Our threat model assumes an attacker can introduce a noise-based perturbation to the raw audio input signal. The goal then is to certify that, for any signal that the attacker can produce, the neural network classifies the signal to the correct label. We perform verification of this property using the framework of abstract interpretation (Gehr et al., 2018). At a high level, the idea is to maintain an abstraction capturing all possible behaviors of both the audio processing stage and the neural network. The flow of DAC is shown in Fig. 1 where all abstractions are dark blue shapes.

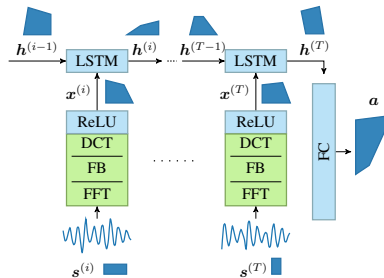


Figure 1: End-to-End Audio Certification Flow using DAC.

Here, all possible signals an attacker can obtain are captured using an abstraction $s^{(i)}$ (a convex relaxation). This abstraction is then propagated through the audio processing stage (shown in green boxes). The key components of this step are *abstract transformers*. For each audio processing operation (e.g. FFT) we create an abstract transformer which receives an abstraction representing an approximation of all possible inputs to the operation and outputs a new abstraction which approximates all possible outputs of the operation. The result of the audio processing stage is the abstraction $x^{(i)}$.

The shape $x^{(i)}$ is then used as input to the recurrent LSTM unit (light blue) which maintains an abstraction of a hidden state $h^{(i-1)}$. LSTM consists of multiple operations and we create a custom abstract transformer for each of those. The result of the transformers in LSTM is a new hidden state $h^{(i)}$. If this was the last frame in the signal (meaning $i = T$), then hidden state $h^{(T)}$ is passed through the fully connected layer of the neural network and, again using the abstract transformer, the final abstract shape a is obtained at the output (at the right of Fig. 1). Finally, to certify the property we check if each concrete output in the abstraction a classifies to the correct label (this is typically easy). If this is true, the output of the network is correct for all inputs that the attacker can create.

Related work on RNN certification The work of (Ko et al., 2019) proposes the POPQORN verifier for recurrent neural networks (RNN). We note that POPQORN does not handle the audio preprocessing pipeline. Even though POPQORN cannot directly verify audio classifiers, their approximations for LSTM non-linearities can be integrated in DAC. This results in $\approx 200\times$ slowdown with small decrease in the volume of the approximation. The massive slowdown makes their approximations unsuitable for certifying audio classifiers. In contrast, using our custom abstract transformers for LSTM non-linearities, DAC can precisely certify end-to-end robustness of challenging audio classifiers in few minutes.

Our main contributions are:

1. A novel and efficient method to certify robustness of neural network audio classifiers to noise-based perturbations. The method is based on new abstract transformers which handle non-linear operations used in both audio processing and recurrent architectures.
2. An implementation of both verification and provably robust training in a system called DAC. We evaluated DAC on common audio classification benchmarks, showing it scales to realistic networks and is far more precise (97% to 2%) than the next best scalable method.

2 BACKGROUND

We first define a threat model that we work with and then present all operations that are part of the verification procedure, including audio processing (MFCC) and LSTM updates. We also discuss the type of verification method we employ.

Threat model We follow the same attacker threat model as Carlini & Wagner (2018). The assumption is that the attacker can add noise δ to the original signal s so to obtain a perturbed signal $s' = s + \delta$. The measure of signal distortion are decibels (dB) defined as:

$$dB(s) = \max_i 20 \cdot \log_{10}(|s_i|); \quad dB_s(\delta) = dB(\delta) - dB(s)$$

Note that the quieter the noise is, the smaller the decibel of perturbation $dB_s(\delta)$ (it is usually a negative value as it is quieter than the signal). We assume the attacker can generate noise δ such that $dB_s(\delta) < \epsilon$ where ϵ is a constant defined by the threat model. Our goal is to verify whether the neural network classifies s' correctly for each small perturbation δ (as constrained above).

Mel-Frequency Cepstral Coefficients (MFCC) *Mel-Frequency Cepstrum* (MFC) is often used for audio preprocessing in speech recognition systems e.g., DeepSpeech (Hannun et al., 2014). The idea of MFC is to model non-linear human acoustic perception as power spectrum filters based on certain frequencies, called *Mel-frequencies*. The final result of the transformation is a vector of coefficients whose elements contain log-scaled values of filtered spectra, one for every Mel-frequency. This resulting vector is a feature representation of the original signal and can now be used in a downstream task such as audio classification.

Sahidullah & Saha (2012) presented an approach to represent MFCC computation using several matrix operations which we integrate with our verification framework. Given T frames of audio signals of

the length $N = 2^k$, represented as matrix $\mathbf{S} = [\mathbf{s}^{(1)} \dots \mathbf{s}^{(T)}]^{tr} \in \mathbb{R}^{T \times N}$ (tr for transpose), audio preprocessing with MFCC is calculated using the following steps:

1. *Pre-emphasizing and Windowing*: $\mathbf{Y} = \mathbf{S}(\mathbf{I}_N - c_{pe}\mathbf{I}_N^{+1}) \odot \mathbf{H}$
Transform the signal with the pre-emphasizing and applying the Hamming window. Here, $\mathbf{I}_N^{+1} \in \mathbb{R}^{N \times N}$ is the shifted diagonal identity matrix ($I_{i,j}^{+1} = 1$ if $i + 1 = j$, otherwise 0), $\mathbf{H} \in \mathbb{R}^{T \times N}$ is the Hamming window, and c_{pe} is the pre-emphasizing constant.
2. *Power Spectrum of Fast Fourier Transform (FFT)*: $\Theta = (\mathbf{Y}\mathbf{W}) \odot (\mathbf{Y}\mathbf{W})$
Perform FFT on the windowed data and square it to get the real-value spectrum. We can denote FFT on discrete domain (DFT) with the multiplication of \mathbf{Y} and $\mathbf{W} \in \mathbb{C}^{N \times N/2}$.
3. *Filter Bank Log Energy*: $\Psi = \log(\Theta\Lambda)$
Apply the Mel frequency filter bank to the power spectrum and get the log value of them. $\Lambda \in \mathbb{R}^{N/2 \times p}$ is the filter bank given the number of filters p , and \log is applied entry-wise.
4. *DCT(Discrete Cosine Transformation)*: $\mathbf{X} = \Psi\mathbf{D}$
Perform DCT on the previous result. Again, this can be formulated using matrix multiplication. We use the resulting $\mathbf{X} = [\mathbf{x}^{(1)} \dots \mathbf{x}^{(T)}]^{tr}$ as the input for the neural network.

Long-Short Term Memory (LSTM) LSTM architectures (Hochreiter & Schmidhuber, 1997) are a key part in modern state-of-the-art speech recognition systems (Hannun et al., 2014; Amodei et al., 2016). In our work, we consider the following definitions of updates in the LSTM unit.

$$\begin{aligned} \mathbf{f}_0^{(t)} &= [\mathbf{x}^{(t)}, \mathbf{h}^{(t-1)}]\mathbf{W}_f + \mathbf{b}_f & \mathbf{o}_0^{(t)} &= [\mathbf{x}^{(t)}, \mathbf{h}^{(t-1)}]\mathbf{W}_o + \mathbf{b}_o \\ \mathbf{i}_0^{(t)} &= [\mathbf{x}^{(t)}, \mathbf{h}^{(t-1)}]\mathbf{W}_i + \mathbf{b}_i & \tilde{\mathbf{c}}_0^{(t)} &= [\mathbf{x}^{(t)}, \mathbf{h}^{(t-1)}]\mathbf{W}_{\tilde{c}} + \mathbf{b}_{\tilde{c}} \\ \mathbf{c}^{(t)} &= \sigma(\mathbf{f}_0^{(t)}) \odot \mathbf{c}^{(t-1)} + \sigma(\mathbf{i}_0^{(t)}) \odot \tanh(\tilde{\mathbf{c}}_0^{(t)}) & \mathbf{h}^{(t)} &= \sigma(\mathbf{o}_0^{(t)}) \odot \tanh(\mathbf{c}^{(t)}) \end{aligned}$$

where $[\cdot, \cdot]$ is the horizontal concatenation two row vectors, \mathbf{W} and \mathbf{b} are kernel and bias of the cell, respectively. At timestep t , vectors $\mathbf{f}_0^{(t)}$, $\mathbf{i}_0^{(t)}$, $\mathbf{o}_0^{(t)}$, $\tilde{\mathbf{c}}_0^{(t)}$ represent pre-activations of the forget, input, and output gate, respectively, and the pre-calculation of cell state. Cell state $\mathbf{c}^{(t)}$ and hidden state $\mathbf{h}^{(t)}$ computed at timestep t are propagated to the LSTM unit at the next timestep, thus allowing it to maintain states. This recurrent architecture allows inputs with arbitrary length, making it especially suited for audio inputs.

Robustness certification In this work, our goal will be to certify the robustness of an audio classification pipeline (including the LSTM) to noise perturbations of the input. To build such a verifier, we leverage the general method of abstract interpretation suggested by Cousot & Cousot (1977), successfully employed by some of the most recent state-of-the-art verifiers of neural networks (Gehr et al., 2018; Singh et al., 2019a). The basic idea here will be to propagate the possible perturbations (captured by a convex region) through the operations of the entire audio pipeline and to then use the final output region to certify the robustness property. The most challenging step of this approach is defining efficient yet precise approximations of the non-linear operations (called abstract transformers) used in the audio pipeline. In this work, we will introduce a number of such new abstract transformers that handle the non-linear operations used in audio processing. Specifically, our over-approximations will be expressed in the recent DEEPPOLY abstraction (Singh et al., 2019a) (a restricted form of convex polyhedra) which aims to balance efficiency and precision. That is, the abstract transformer of a non-linear function will take as input a convex polyhedra element expressible in DEEPPOLY and output another polyhedra which over-approximates the behavior of the non-linear operation when invoked with any concrete point inside the original polyhedra.

3 OVERVIEW OF VERIFICATION PROCESS

We now explain the workings of our verifier on a (toy) example from the point where sound enters the processing stage to where the output of the classifier is certified as robust under any allowed perturbation of the threat model. Our goal is to provide an intuitive understanding, formal details are provided later.

Audio preprocessing Unlike in standard computer vision tasks where the input is fed directly to the neural network, audio models typically first perform MFCC preprocessing to extract useful features

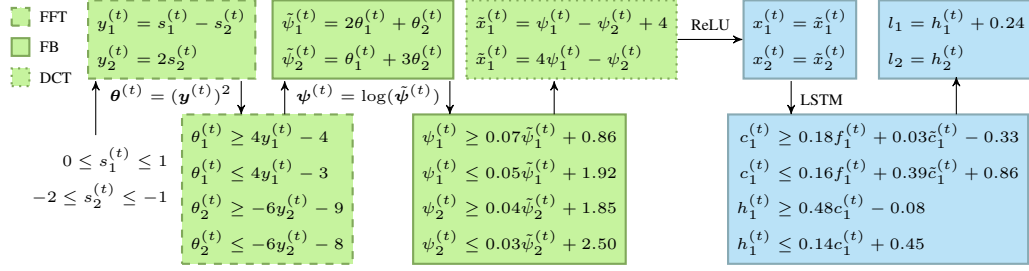


Figure 2: Robustness verification illustrated on a toy example. Each box shows the constraints computed by the verifier after processing a given operation (shown on edges). Green color denotes elements of the MFCC audio processing stage: the Fast Fourier Transform (FFT), the Filterbank Transform (FB), and the Discrete Cosine Transform (DCT). Blue color denotes components of the network: ReLU layer, LSTM and Fully Connected layer. Approximations computed with this work are shown in the bottom row. The operations which the abstract transformers handle are shown next to the downward edges. Edges without labels represent affine transforms.

from the signal. We represent all preprocessing operations as green boxes in Fig. 2. The calculation follows steps described formally in Section 2, using the same notation for resulting vectors.

Fast Fourier transform The first operation is Fast Fourier Transform (FFT) of the pre-emphasized input signal. It is a two-step process shown in dashed boxes in Fig. 2. We decompose it into affine and square operations which transform signal $s^{(t)}$ into an intermediate representation $\theta^{(t)}$. Using our novel and optimal abstract transformer for the square operation, formally defined in Section 4 and visualized in Fig. 3b, we obtain linear bounds on $\theta^{(t)}$.

Filterbank transform The next operation is Filterbank transform (FB) which consists of affine and logarithm operations, shown in solid boxes in Fig. 2. Note that if the approximations from the square transformer allows negative values, then the entire analysis will fail as the logarithm operation is undefined for negative inputs. Our transformers are carefully designed to avoid this scenario. To obtain bounds on the output of the logarithm we apply our novel and optimal logarithm transformer, also formally described in Section 4 and visualized in Fig. 3a, and obtain linear upper and lower bounds on the log energy of the filtered power spectrum, $\psi^{(t)}$. Logarithm operation is followed by Discrete Cosine Transform (DCT) resulting in a vector $\tilde{x}^{(t)}$ which is then used as an input to the fully connected layer of the neural network followed by a ReLU. Our analysis (detailed calculation in Appendix C) produces $\tilde{x}_1^{(t)} \in [0.87, 5.56]$, $\tilde{x}_2^{(t)} \in [0.17, 12.8]$. Since all the values are positive, the following ReLU has no effect on its input and thus we set $x^{(t)} = \tilde{x}^{(t)}$. Using the back-substitution technique we describe later, we derive $x_1^{(t)} \in [0.87, 5.56]$, $x_2^{(t)} \in [0.17, 12.83]$. In the next paragraph we describe bound propagation through LSTM in more detail.

LSTM bound propagation Here we provide a technical overview of our LSTM transformer, formalized in Section 5 and visualized in Fig. 4, by calculating the result of the transformation on the first neuron of the LSTM hidden layer. We provide detailed mathematical basis of this process in Appendix D. For our toy example, let the gates be updated as $f_1^{(t)} = x_1^{(t)}/4$, input gate $i_1^{(t)} = 2h_2^{(t-1)}$, output gate $o_1^{(t)} = h_1^{(t-1)}$ and cell state $\tilde{c}^{(t)} = h_1^{(t-1)} - x_2^{(t)}/4$. Also, assume the previous states are bounded by: $h_1^{(t-1)}, h_2^{(t-1)}, c_1^{(t-1)}, c_2^{(t-1)} \in [0.90, 1.00]$. We now apply our $\sigma(x) \cdot \tanh(y)$ and $\sigma(x) \cdot y$ transformers to get bounds of the cell state $c_1^{(t)} = \sigma(f_1^{(t)}) \cdot c_1^{(t-1)} + \sigma(i_1^{(t)}) \cdot \tanh(\tilde{c}_1^{(t)})$.

$$\begin{aligned} 0.18f_1^{(t)} + 0.45 &\leq \sigma(f_1^{(t)}) \cdot c_1^{(t-1)} \leq 0.16f_1^{(t)} + 0.58 \\ 0.03\tilde{c}_1^{(t)} - 0.78 &\leq \sigma(i_1^{(t)}) \cdot \tanh(\tilde{c}_1^{(t)}) \leq 0.39\tilde{c}_1^{(t)} + 0.28 \end{aligned}$$

Summing up the inequalities above results in $c_1^{(t)} \in [-0.36, 1.46]$. For the hidden state $h_1^{(t)} = \sigma(o_1^{(t)}) \cdot \tanh(c_1^{(t)})$, we again apply our abstract transformer and obtain

$$0.48c_1^{(t)} - 0.08 \leq \sigma(o_1^{(t)}) \cdot \tanh(c_1^{(t)}) \leq 0.14c_1^{(t)} + 0.45$$

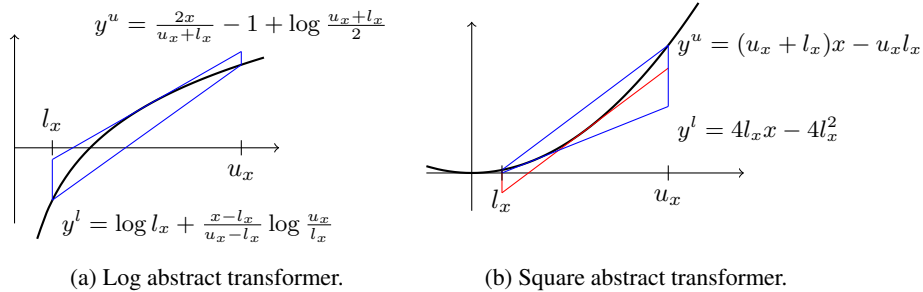


Figure 3: Our DeepPoly approximations of (a) the natural logarithm and (b) the square function. Blue lines represent the valid (in case of square, non-negative) upper and lower bounds which minimize the area between the planes under the given domain $[l_x, u_x]$. The red bound on (b) grants smaller area, but contains the negative value, which occurs the analysis failure in the audio processing pipeline.

i.e., $h_1^{(t)} \in [-0.25, 0.65]$. An analogous computation is performed for $h_2^{(t)}$. For this example, we assume the computation results in $h_2^{(t)} = 0$.

Robustness certification using DeepPoly The hidden states in the LSTM at the final timestep are passed through a fully connected layer without activation. In our example we assume that logits after the layer are obtained with the following formula: $l_1 = h_1^{(t)} + 0.24$ and $l_2 = h_2^{(t)}$. These are shown in the final box of Fig. 2. To certify that the neural network classifies the input to class 1, we need to prove that $l_1 - l_2 > 0$. We now apply the back-substitution technique as in Singh et al. (2019a) upto the input to the LSTM:

$$\begin{aligned} l_1 - l_2 &= h_1^{(t)} - h_2^{(t)} + 0.24 \geq 0.48(0.18f_1^{(t)} + 0.03\tilde{c}_1^{(t)} - 0.33) - 0.08 + 0.24 \\ &= 0.09f_1^{(t)} + 0.01\tilde{c}_1^{(t)} + 0.01 = 0.09(x_1^{(t)}/4) + 0.01(h_1^{(t-1)} - x_2^{(t)}/4) + 0.01 \geq 0.006 \end{aligned}$$

As this value is greater than 0, robustness is established. In Appendix C we show more detailed calculations to obtain tighter bound 0.0375 by also back-substituting in the preprocessing pipeline. For our experiments in Section 6, we tune the number of backsubstitution steps to achieve a good tradeoff between speed and precision. Note that robustness cannot be proved if one concretizes the expression above to an interval, instead of performing back-substitution of linear bounds. For instance, if we concretize $h_1^{(t)}$ to $[-0.25, 0.65]$, we obtain $l_1 - l_2 \geq h_1^{(t)} - h_2^{(t)} + 0.24 \geq -0.01$ which is imprecise and fails to certify robustness. Note that if t is not the last timestep, the hidden state and the cell state are passed to the next analysis timestep instead of computing the final output.

4 AUDIO PROCESSING TRANSFORMERS

As illustrated earlier, the first part of the verification process involves handling of the audio processing stage (performed using MFCC). Here, most matrix multiplication parts can be captured exactly by our abstraction, but MFCC also includes the square operation in the FFT and the logarithm operation in the computation of energy from filterbanks. Thus, to handle these non-linear operations, we need to create new abstract transformers, which we present next. To ensure a minimal loss of precision, our abstract transformers minimize the area between the lower and upper bounds in the input-output plane. This approach of minimizing the area has been used before for other transformers and has been shown to be practically effective in Singh et al. (2018; 2019a).

We denote the set of all variables in the analysis as \mathcal{X} . For an element $x \in \mathcal{X}$, we denote the functions corresponding to its linear lower and upper bound as x^l and x^u , respectively. These are scalar functions defined on \mathbb{R}^k where k is the number of other variables used to compute x . For every element, we also maintain interval bounds, $x \in [l_x, u_x]$. For ease of explanation, we introduce the log transformer followed by the square transformer.

Log abstract transformer The logarithm operation is an assignment $y := \log(x)$ where $x, y \in \mathcal{X}$. The output of this operation cannot be captured exactly and we need to carefully introduce an approximation. Here, we first compute the minimum $l_y = \log(l_x)$ and the maximum $u_y = \log(u_x)$,

which we use as interval approximation. We define linear lower and upper bound functions $y^l, y^u : \mathbb{R} \rightarrow \mathbb{R}$. Using concavity of the logarithm on any subset of the domain, the lower bound function is a line connecting the points $(l_x, \log(l_x))$ and $(u_x, \log(u_x))$. The upper bound function is chosen as the tangent line to the function minimizing the area between the lower and the upper bound. As a result, we obtain the following bounds as depicted in Fig. 3a:

$$y^l(x) = \log l_x + \frac{x - l_x}{u_x - l_x} \log \frac{u_x}{l_x} \quad y^u(x) = \frac{2x}{u_x + l_x} - 1 + \log \frac{u_x + l_x}{2}$$

Note that if $l_x \leq 0$, $y^l(x) = -\infty$ since the function is not defined on that domain. We make an exception when $u_x - l_x < 10^{-4}$ to use interval bound for y^l for avoiding the unstable floating point calculation caused by large denominator of x coefficient.

Square abstract transformer The square operation is an assignment $y := x^2$ where $x, y \in \mathcal{X}$. Similar to logarithm, this operation is non-linear and cannot be captured exactly in the abstraction. We first compute the interval bounds of the output l_y and u_y , and set the minimum value l_y to 0 when $0 \in [l_x, u_x]$ and $\min(l_x^2, u_x^2)$ otherwise. The maximum value u_y is simply $\max(l_x^2, u_x^2)$.

Next, we define linear lower and upper bound functions $y^l, y^u : \mathbb{R} \rightarrow \mathbb{R}$. Using the convexity of the square function, we set the upper bound function y^u to the linear function connecting (l_x, l_x^2) and (u_x, u_x^2) . For the lower bound function y^l , we have to be delicate: since $x^2 : \mathbb{R} \rightarrow \mathbb{R}^{\geq 0}$, our y^l should also be greater or equal than 0 within any domain. With the principle of minimizing the area between the bounds, we obtain the following bounds for cases as shown in Fig. 3b:

$$y^l(x) = \begin{cases} 4l_x x - 4l_x^2 & 0 \leq l_x < u_x/3 \\ 4u_x x - 4u_x^2 & 0 \geq l_x > 3u_x \\ 0 & l_x \leq 0 \leq u_x \\ (u_x + l_x)x - ((u_x + l_x)/2)^2 & otherwise \end{cases} \quad y^u(x) = (u_x + l_x)x - u_x l_x$$

5 LSTM TRANSFORMERS

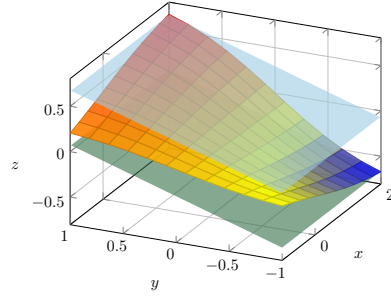
Most prior work on verification of neural networks focuses on feed-forward or convolutional architectures whose operations consist of a sequence of affine transforms and activation functions. However, to perform verification of recurrent architectures, one needs to handle the updates of the recurrent unit. Following the equations updating the LSTM presented in Section 2, we can observe that pre-activations of gates are affine transforms which can be captured exactly in our abstraction. However, the operations updating the cell and hidden states are non-linear and require approximation.

Overall, we have three elementwise products – two are between a sigmoid and a tanh and one between a sigmoid and the identity. A straightforward approach to handling such transforms would be to concretize the polyhedra DeepPoly element to an interval and perform the multiplication using intervals. However, this approach would lose all relations between inputs and incur precision loss in future operations of the analysis. Instead, we design custom binary approximation transformers specifically tailored to handle the elementwise product in the update of the recurrent unit.

Sigmoid \odot Tanh abstract transformer We define elementwise multiplication between sigmoid and tanh as an assignment $z := \sigma(x) \tanh(y)$, where $x, y, z \in \mathcal{X}$. As before, our aim is to construct linear bounds z^l, z^u . Unlike the previously defined DeepPoly transformers which take as input a single abstract element, this transformer is the first which receives two abstract elements as operands. Hence, the bound functions have the form $z^l, z^u : \mathbb{R}^2 \rightarrow \mathbb{R}$.

Let $z = f(x, y) = \sigma(x) \cdot \tanh(y)$. Our goal is to bound this function between two planes such that the volume between the planes is as small as possible (following our previous heuristic). We first divide the computation into 3 cases based on the signs of l_y and u_y . To simplify notation, we introduce the variable assignment in Table 1 so that we can reuse notation across all cases. We first define an *anchor* point \mathbf{a} : a point in the box $[l_x, u_x] \times [l_y, u_y]$ where function f attains the max/min value defined upon the case. Also we need *reference* point \mathbf{r} whereas the plane would meet first among the four corners if it is tilted in given direction, other than the anchor. Our transformer

| | | z_x^u | z_y^u | z_x^l | z_y^l |
|--------------------|--------------|------------|------------|------------|------------|
| $l_y \geq 0$ | Φ | min | min | min | min |
| | \mathbf{a} | u_x, u_y | u_x, u_y | l_x, l_y | l_x, l_y |
| | \mathbf{r} | l_x, u_y | u_x, l_y | u_x, l_y | l_x, u_y |
| $l_y < 0 \leq u_y$ | Φ | min | min | max | min |
| | \mathbf{a} | u_x, u_y | u_x, u_y | u_x, l_y | u_x, l_y |
| | \mathbf{r} | l_x, u_y | l_x, l_y | l_x, l_y | l_x, u_y |
| $u_y < 0$ | Φ | max | min | max | min |
| | \mathbf{a} | l_x, u_y | l_x, u_y | u_x, l_y | u_x, l_y |
| | \mathbf{r} | u_x, u_y | l_x, l_y | l_x, l_y | u_y, u_y |

Table 1: Variable reference for the $\sigma(x) \cdot \tanh(y)$ approximation.Figure 4: Visualization of the bounding planes and $\sigma(x) \cdot \tanh(y)$ curve.

computes two candidates planes for the upper bound (z_x^u, z_y^u) and two for the lower bound (z_x^l, z_y^l) as:

$$(z^u|z^l)_x = \Phi \left(D_i f(\mathbf{a}), \frac{f(\mathbf{a}) - f(\mathbf{r})}{a_x - r_x} \right) (x - a_x) + f(\mathbf{a})$$

$$(z^u|z^l)_y = \Phi \left(D_j f(\mathbf{a}), \frac{f(\mathbf{a}) - f(\mathbf{r})}{a_y - r_y} \right) (y - a_y) + f(\mathbf{a})$$

where $D_i f = \frac{\partial f}{\partial x}$, $D_j f = \frac{\partial f}{\partial y}$, and Φ , \mathbf{a} , \mathbf{r} are chosen from Table 1. Finally, we choose bounds from two candidates which minimize the volume between the planes. Fig. 4 is the visualization of this result. We note that Sigmoid \odot Identity transformer is handled in the same manner (we can directly apply the same transformer by replacing $f(x, y)$ with $\sigma(x) \cdot y$).

Theorem 1. *Our Sigmoid \odot Tanh transformer is optimal (it minimizes the volume between the lower and upper plane) under the assumptions: (1) bounding planes are tangent to the curve at the respective anchor points, (2) bounding planes are parallel to either x or y axis. Planes computed using our transformer result in a volume strictly smaller than those computed using interval analysis.*

We show the proof in Appendix B. Our assumptions are based on the following reasoning. The first assumption is needed so that our transformer produces bounds strictly better than interval analysis. Unless z^u passes through the point (u_x, u_y) , the concrete upper bound would be larger than $\sigma(u_x) \cdot \tanh(u_y)$, making it worse than an interval bound (analogously for the lower bound). The second assumption enables computation of optimal planes in $O(1)$ while without this assumption one needs to solve a non-convex optimization problem which is not feasible at the scale of networks we consider.

6 EXPERIMENTS

We now evaluate the effectiveness of DAC on several datasets and neural architectures. All our transformers are implemented in C (for performance) and exposed to the verifier using a Python interface. We will publicly release the datasets, trained networks and source code of DAC. Verification is performed on a Intel(R) Core(TM) i9-9900K CPU @ 3.60GHz using 6 cores for each instance.

Experimental setup We evaluate on audio classification benchmarks: Free Spoken Digit Dataset (FSDD) (Jackson, 2019) and Google Speech Commands (GSC) (Warden, 2018). FSDD contains 2,000 samples of spoken digits while GSC is a more complex dataset containing 65,000 utterances of 30 short words spoken by thousands of different people. State-of-the-art accuracy on GSC is 96.9% by de Andrade et al. (2018) using attention RNN, while our verified model achieves 89%.

Robustness evaluation Following Singh et al. (2019b), we define success rate of verification as the ratio between certified samples and correctly predicted ones. We randomly shuffled the test data and then, for every experiment, inferred labels one by one until the number of correctly classified samples reached 100. We report the number of provably correct samples out of these 100 as our provability. As a baseline, we consider a verification method based on interval analysis, which only derives neuronwise lower and upper bounds using the previous layer’s bounds. We used networks with $h = 40$ hidden neurons and $p = 10$ filters for both FSDD and GSC. Our results are shown in Fig. 5.

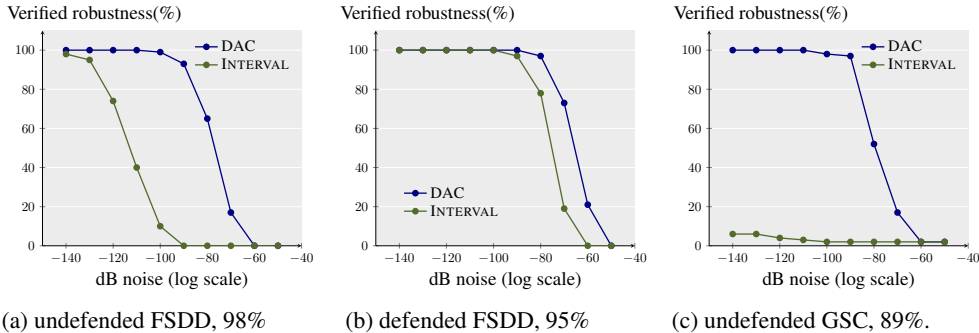


Figure 5: Robustness evaluation on FSDD and GSC datasets, using DAC and Interval analysis.

They suggest that DAC substantially outperforms interval analysis due to better approximations of key functions in both audio preprocessing and neural network stages.

Effect of back-substitution depth In this experiment, we vary the depth of back-substitution used in DAC and study its effect on our performance. We run this experiment on an FSDD network and report the results in Table 2. We observe that increasing the back-substitution depth increases the provability. This is due to the fact that we benefit from cancellation of common terms in the propagated expressions, as demonstrated in our example in Section 3. However, this comes at a cost of exponential increase in runtime. Thus, we choose to use depth 3 in order to get high verification rate while still having reasonable verification speed.

| Depth | Provability(%) | Run Time(s) |
|-------|----------------|-------------|
| 0 | 27 | 8.33 |
| 1 | 35 | 18.95 |
| 2 | 37 | 40.83 |
| 3 | 39 | 87.92 |
| 4 | 40 | 166.19 |
| 5 | 41 | 328.92 |

Table 2: Effect of back-substitution depth on the performance.

Provable defense for audio classifiers We also for the first time trained audio classifiers to be provably robust against noise-based perturbations. Our training follows Mirman et al. (2018); Goyal et al. (2018) – we perturb the input signal and propagate interval bounds through the audio processing and LSTM stages. To train, we combine standard loss with the worst case loss obtained using interval propagation. The resulting network shown in Fig. 5b achieves 80% of provability for -80 dB even with the imprecise interval analysis, outperforming the undefended network. Even though this network was specifically trained to be verifiable using interval analysis, DAC still outperforms interval analysis and proves significantly more robustness properties. Also note that the network trained this way has lower accuracy of 95% compared to the 98% accuracy of the baseline.

Experimental comparison with prior work POPQORN (Ko et al., 2019) also proposes a method to certify recurrent neural networks by propagating linear bounds. One of the key differences with our work is the approximation of $\sigma(x) \cdot \tanh(y)$ using linear bounds. We found that, in practice, optimization approach used by POPQORN produces approximations of slightly smaller volume than our LSTM transformer (although non-comparable). However, this smaller volume comes at a high cost in runtime. We tried to integrate POPQORN bounds into our verification framework, however we found it not feasible for our audio tasks as it increased our end-to-end runtime $200\times$ on one of the smaller networks. In contrast, DAC takes only 1-2 minutes on average to verify a single example containing multiple frames. Indeed, our observation is consistent with the evaluation of POPQORN in the paper where it takes hours on a GPU for verifying NLP and vision tasks only for a single frame.

7 CONCLUSION

We presented the first verifier for certifying audio classifiers. The key idea was to create abstract transformers for non-linear operations used in the audio processing stage and the recurrent network. These transformers compute an optimal (area-wise) approximation under assumptions representable in the underlying convex relaxation and enable sound handling of the entire pipeline. Our evaluation shows that DAC is practically effective and achieves high verification rates on different datasets.

REFERENCES

- Dario Amodei, Sundaram Ananthanarayanan, Rishita Anubhai, Jingliang Bai, Eric Battenberg, Carl Case, Jared Casper, Bryan Catanzaro, Qiang Cheng, Guoliang Chen, et al. Deep speech 2: End-to-end speech recognition in english and mandarin. In *International conference on machine learning*, pp. 173–182, 2016.
- Ross Anderson, Joey Huchette, Will Ma, Christian Tjand raatmadja, and Juan Pablo Vielma. Strong mixed-integer programming formulations for trained neural networks. *arXiv e-prints*, pp. arXiv:1811.01988, 2018.
- Rudy Bunel, Ilker Turkaslan, Philip H.S. Torr, Pushmeet Kohli, and M. Pawan Kumar. A unified view of piecewise linear neural network verification. In *Proc. Advances in Neural Information Processing Systems (NeurIPS)*, pp. 4795–4804, 2018.
- Nicholas Carlini and David Wagner. Audio adversarial examples: Targeted attacks on speech-to-text. In *2018 IEEE Security and Privacy Workshops (SPW)*, pp. 1–7. IEEE, 2018.
- Nicholas Carlini, Pratyush Mishra, Tavish Vaidya, Yuankai Zhang, Micah Sherr, Clay Shields, David Wagner, and Wenchao Zhou. Hidden voice commands. In *25th {USENIX} Security Symposium ({USENIX} Security 16)*, pp. 513–530, 2016.
- Chung-Cheng Chiu, Tara N. Sainath, Yonghui Wu, Rohit Prabhavalkar, Patrick Nguyen, Zhifeng Chen, Anjuli Kannan, Ron J. Weiss, Kanishka Rao, Katya Gonina, Navdeep Jaitly, Bo Li, Jan Chorowski, and Michiel Bacchiani. State-of-the-art speech recognition with sequence-to-sequence models. *CoRR*, abs/1712.01769, 2017. URL <http://arxiv.org/abs/1712.01769>.
- Patrick Cousot and Radhia Cousot. Abstract interpretation: a unified lattice model for static analysis of programs by construction or approximation of fixpoints. In *Proceedings of the 4th ACM SIGACT-SIGPLAN symposium on Principles of programming languages*, pp. 238–252. ACM, 1977.
- Douglas Coimbra de Andrade, Sabato Leo, Martin Loesener Da Silva Viana, and Christoph Bernkopf. A neural attention model for speech command recognition. *arXiv preprint arXiv:1808.08929*, 2018.
- Krishnamurthy Dvijotham, Robert Stanforth, Sven Gowal, Timothy Mann, and Pushmeet Kohli. A dual approach to scalable verification of deep networks. In *Proc. Uncertainty in Artificial Intelligence (UAI)*, pp. 162–171, 2018.
- Krishnamurthy (Dj) Dvijotham, Robert Stanforth, Sven Gowal, Chongli Qin, Soham De, and Pushmeet Kohli. Efficient neural network verification with exactness characterization. In *Proc. Uncertainty in Artificial Intelligence, UAI*, pp. 164, 2019.
- Rüdiger Ehlers. Formal verification of piece-wise linear feed-forward neural networks. In *Automated Technology for Verification and Analysis (ATVA)*, 2017.
- Mohammad Esmailpour, Patrick Cardinal, and Alessandro Lameiras Koerich. A robust approach for securing audio classification against adversarial attacks. *arXiv preprint arXiv:1904.10990*, 2019.
- Timon Gehr, Matthew Mirman, Dana Drachler-Cohen, Petar Tsankov, Swarat Chaudhuri, and Martin Vechev. Ai2: Safety and robustness certification of neural networks with abstract interpretation. In *2018 IEEE Symposium on Security and Privacy (SP)*, pp. 3–18. IEEE, 2018.
- Ian J Goodfellow, Jonathon Shlens, and Christian Szegedy. Explaining and harnessing adversarial examples. *arXiv preprint arXiv:1412.6572*, 2014.
- Sven Gowal, Krishnamurthy Dvijotham, Robert Stanforth, Rudy Bunel, Chongli Qin, Jonathan Uesato, Timothy Mann, and Pushmeet Kohli. On the effectiveness of interval bound propagation for training verifiably robust models. *arXiv preprint arXiv:1810.12715*, 2018.
- Alex Graves, Abdel-rahman Mohamed, and Geoffrey Hinton. Speech recognition with deep recurrent neural networks. In *2013 IEEE international conference on acoustics, speech and signal processing*, pp. 6645–6649. IEEE, 2013.

- Awni Hannun, Carl Case, Jared Casper, Bryan Catanzaro, Greg Diamos, Erich Elsen, Ryan Prenger, Sanjeev Satheesh, Shubho Sengupta, Adam Coates, et al. Deep speech: Scaling up end-to-end speech recognition. *arXiv preprint arXiv:1412.5567*, 2014.
- Sepp Hochreiter and Jürgen Schmidhuber. Long short-term memory. *Neural Comput.*, 9(8):1735–1780, November 1997. ISSN 0899-7667. doi: 10.1162/neco.1997.9.8.1735. URL <http://dx.doi.org/10.1162/neco.1997.9.8.1735>.
- Zohar Jackson. Free spoken digit dataset. <https://github.com/Jakobovski/free-spoken-digit-dataset>, 2019.
- Guy Katz, Clark Barrett, David L Dill, Kyle Julian, and Mykel J Kochenderfer. Reluplex: An efficient smt solver for verifying deep neural networks. In *International Conference on Computer Aided Verification*, pp. 97–117. Springer, 2017.
- CY Ko, Z Lyu, TW Weng, L Daniel, N Wong, and D Lin. Popqorn: Certifying robustness of recurrent neural networks. In *International Conference on Machine Learning (ICML)*, 2019.
- Matthew Mirman, Timon Gehr, and Martin Vechev. Differentiable abstract interpretation for provably robust neural networks. In *International Conference on Machine Learning*, pp. 3575–3583, 2018.
- Paarth Neekhara, Shehzeen Hussain, Prakhar Pandey, Shlomo Dubnov, Julian McAuley, and Farinaz Koushanfar. Universal adversarial perturbations for speech recognition systems. *arXiv preprint arXiv:1905.03828*, 2019.
- Yao Qin, Nicholas Carlini, Ian Goodfellow, Garrison Cottrell, and Colin Raffel. Imperceptible, robust, and targeted adversarial examples for automatic speech recognition. In *International Conference on Machine Learning (ICML)*, 2019.
- Aditi Raghunathan, Jacob Steinhardt, and Percy S Liang. Semidefinite relaxations for certifying robustness to adversarial examples. In *Advances in Neural Information Processing Systems (NeurIPS)*, pp. 10877–10887. 2018.
- Wenjie Ruan, Xiaowei Huang, and Marta Kwiatkowska. Reachability analysis of deep neural networks with provable guarantees. In *Proc. International Joint Conference on Artificial Intelligence, IJCAI*, pp. 2651–2659, 2018.
- Md Sahidullah and Goutam Saha. Design, analysis and experimental evaluation of block based transformation in mfcc computation for speaker recognition. *Speech Communication*, 54(4): 543–565, 2012.
- Hadi Salman, Greg Yang, Huan Zhang, Cho-Jui Hsieh, and Pengchuan Zhang. A convex relaxation barrier to tight robustness verification of neural networks. *CoRR*, abs/1902.08722, 2019.
- Gagandeep Singh, Timon Gehr, Matthew Mirman, Markus Püschel, and Martin Vechev. Fast and effective robustness certification. In *Advances in Neural Information Processing Systems*, pp. 10802–10813, 2018.
- Gagandeep Singh, Timon Gehr, Markus Püschel, and Martin Vechev. An abstract domain for certifying neural networks. *Proceedings of the ACM on Programming Languages*, 3(POPL):41, 2019a.
- Gagandeep Singh, Timon Gehr, Markus Püschel, and Martin Vechev. Boosting robustness certification of neural networks. In *International Conference on Learning Representations*, 2019b.
- Christian Szegedy, Wojciech Zaremba, Ilya Sutskever, Joan Bruna, Dumitru Erhan, Ian Goodfellow, and Rob Fergus. Intriguing properties of neural networks. *arXiv preprint arXiv:1312.6199*, 2013.
- Vincent Tjeng, Kai Y. Xiao, and Russ Tedrake. Evaluating robustness of neural networks with mixed integer programming. In *International Conference on Learning Representations, (ICLR)*, 2019.
- Shiqi Wang, Kexin Pei, Justin Whitehouse, Junfeng Yang, and Suman Jana. Efficient formal safety analysis of neural networks. In *Advances in Neural Information Processing Systems*, pp. 6367–6377, 2018.

- Pete Warden. Speech commands: A dataset for limited-vocabulary speech recognition. *arXiv preprint arXiv:1804.03209*, 2018.
- Lily Weng, Huan Zhang, Hongge Chen, Zhao Song, Cho-Jui Hsieh, Luca Daniel, Duane Boning, and Inderjit Dhillon. Towards fast computation of certified robustness for ReLU networks. In *Proc. International Conference on Machine Learning (ICML)*, volume 80, pp. 5276–5285, 2018.
- Eric Wong, Frank R. Schmidt, Jan Hendrik Metzen, and J. Zico Kolter. Scaling provable adversarial defenses. In *Proc. Neural Information Processing Systems (NeurIPS)*, pp. 8410–8419, 2018.
- Zhuolin Yang, Bo Li, Pin-Yu Chen, and Dawn Song. Characterizing audio adversarial examples using temporal dependency. 2019.
- Guoming Zhang, Chen Yan, Xiaoyu Ji, Tianchen Zhang, Taimin Zhang, and Wenyuan Xu. Dolphinnattack: Inaudible voice commands. In *Proceedings of the 2017 ACM SIGSAC Conference on Computer and Communications Security*, pp. 103–117. ACM, 2017.
- Huan Zhang, Tsui-Wei Weng, Pin-Yu Chen, Cho-Jui Hsieh, and Luca Daniel. Efficient neural network robustness certification with general activation functions. In *Advances in Neural Information Processing Systems*, pp. 4939–4948, 2018.

A SOUNDNESS PROOF OF SIGMOID \odot TANH ABSTRACT TRANSFORMER

Suppose x and y are the abstract variable bounded by $[l_x, u_x], [l_y, u_y]$ respectively. This suggested transformer finds the bounding planes of the function $f(x, y) = \sigma(x) \tanh(y)$. Let $D_i f = \frac{\partial f}{\partial x}$ and $D_j f = \frac{\partial f}{\partial y}$.

1. $l_y \geq 0$

Choose the upper bound of the function between z_x^u and z_y^u , where

$$z_x^u(x, y) = \min \left(D_i f(u_x, u_y), \frac{f(u_x, u_y) - f(l_x, u_y)}{u_x - l_x} \right) (x - u_x) - f(u_x, u_y)$$

$$z_y^u(x, y) = \min \left(D_j f(u_x, u_y), \frac{f(u_x, u_y) - f(u_x, l_y)}{u_y - l_y} \right) (y - u_y) - f(u_x, u_y)$$

by the smaller volume under the each plane.

Claim 1: $z_x^u(x, y) \geq f(x, y)$ in $(x, y) \in [l_x, u_x] \times [l_y, u_y]$.

Let $x_1 < x_2 \in [l_x, u_x]$ and $y_1 < y_2 \in [l_y, u_y]$. Then for any x, y , $f(x, y_1) < f(x, y_2)$ and $f(x_1, y) < f(x_2, y)$. Thus, since z_x^u is independent to y , it is sufficient to show $z_x^u(x, \cdot) \geq f(x, u_y)$.

We can easily know that $f(x, u_y)$ is concave at $x \geq 0$ and convex at $x \leq 0$ by the second derivation of f .

- (a) Consider the case of $u_x > 0$. Let x_0 be the x coordinate of the crossing of $f(x, u_y)$ and $g(x) = D_i f(u_x, u_y)(x - u_x) - f(u_x, u_y)$. From the convexity of $f(x, u_y)$ in $x < 0$, $g(0) > f(0, u_y)$, and $g'(x) > 0$, there exists a single $x_0 < 0$. If $l_x > x_0$, the slope of $z_x^u(x, \cdot)$ becomes $D_i f(u_x, u_y)$, and z_x^u and g become identical. Hence, $f(x, u_y) \leq g(x) = z_x^u(x, \cdot)$. If $l_x \leq x_0$, the slope of $z_x^u(x, \cdot)$ becomes $\frac{f(u_x, u_y) - f(l_x, u_y)}{u_x - l_x}$. Then z_x^u and g shares a point of u_x but z_x^u has smaller slope, so $g(x) \leq z_x^u(x, \cdot)$ in $[l_x, u_x]$. Also from $f(l_x, u_y) = z_x^u(l_x, \cdot)$ and $f(0, u_y) < z_x^u(0, \cdot)$, $f(x, u_y) \leq z_x^u(x, \cdot)$. Thus, the claim holds when $u_x > 0$.
- (b) Another case of $u_x \leq 0$, x coefficient of z_x^u will always be $\frac{f(u_x, u_y) - f(l_x, u_y)}{u_x - l_x}$. Again, by convexity of $f(x, u_y)$, $z_x^u(x, \cdot) \geq f(x, u_y)$.

Hence $z_x^u(x, \cdot) \geq f(x, u_y) \geq f(x, y)$ holds in $(x, y) \in [l_x, u_x] \times [l_y, u_y]$. Claim proved.

With analogous steps, z_y^u can be shown to cover above the curve. Choosing the plane with smaller volume underneath it allows to minimize the expected difference between the true curve and the upper bound plane under the randomly chosen domain.

For the lower bound, choose the upper bound of the function between z_x^l and z_y^l , where

$$z_x^l(x, y) = \min \left(D_i f(l_x, l_y), \frac{f(l_x, l_y) - f(u_x, l_y)}{l_x - u_x} \right) (x - l_x) - f(l_x, l_y)$$

$$z_y^l(x, y) = \min \left(D_j f(l_x, l_y), \frac{f(l_x, l_y) - f(l_x, u_y)}{l_y - u_y} \right) (y - l_y) - f(l_x, l_y)$$

by the larger volume under the each plane.

Claim 2: $z_x^l(x, y) \leq f(x, y)$ in $(x, y) \in [l_x, u_x] \times [l_y, u_y]$.

It is sufficient to show $z_x^l(x, \cdot) \geq f(x, l_y)$ since $f(x, y_1) \leq f(x, y_2)$ for $y_1 \leq y_2$.

- (a) Consider the case of $l_x < 0$. Let x_0 be the x coordinate of the crossing of $f(x, l_y)$ and $g(x) = D_i f(l_x, l_y)(x - l_x) - f(l_x, l_y)$. From the concavity of $f(x, l_y)$ in $x > 0$, $g(0) < f(0, l_y)$, and $g'(x) > 0$, there exists a single $x_0 > 0$. If $l_x < x_0$, the slope of $z_x^l(x, \cdot)$ becomes $D_i f(l_x, l_y)$, and z_x^l and g become identical. Hence, $f(x, l_y) \leq g(x) = z_x^l(x, \cdot)$. If $l_x \geq x_0$, the slope of $z_x^l(x, \cdot)$ becomes $\frac{f(l_x, l_y) - f(u_x, l_y)}{l_x - u_x}$. Then z_x^l and g shares a point of l_x but z_x^l has smaller slope, so $g(x) \geq z_x^l(x, \cdot)$ in $[l_x, u_x]$. Also from $f(u_x, l_y) = z_x^l(u_x, \cdot)$ and $f(0, l_y) > z_x^l(0, \cdot)$, $f(x, l_y) \geq z_x^l(x, \cdot)$. Thus, the claim holds when $u_x < 0$.

- (b) Another case of $l_x \geq 0$, x coefficient of z_x^l will always be $\frac{f(l_x, l_y) - f(u_x, l_y)}{l_x - u_x}$. Again, by convexity of $f(x, l_y)$, $z_x^l(x, \cdot) \leq f(x, l_y)$.

Hence $z_x^l(x, \cdot) \leq f(x, l_y) \geq f(x, y)$ holds in $(x, y) \in [l_x, u_x] \times [l_y, u_y]$. Claim proved.

With analogous steps, z_y^l can be shown to lie under the curve. Choosing the plane with larger volume underneath it allows to minimize the expected difference between the true curve and the lower bound plane under the randomly chosen domain.

2. $l_y \leq 0 \leq u_y$

The proof of upper bounds will follow the same steps with the first case. z_x^u in this case is exactly same as before, but since $f(x, y)$ goes below 0 when $y < 0$, z_y^u has to anchor at (l_x, l_y) instead of (u_x, l_y) since $f(l_x, l_y) \geq f(u_x, l_y)$ and convexity of f in the region. The proof steps do not differ much from the previous proofs.

Again, the proof for lower bound is similar as before, but note that z_x^l needs to choose *maximum* between the two slopes. This is due to the sign of the values. Since $f(u_x, l_y) < 0$ is the minimum in the region and it grows along x gets smaller, both $D_x f(u_x, l_y)$ and $\frac{f(u_x, l_y) - f(l_x, l_y)}{u_x - l_x}$ are less than zero.

3. $0 \geq u_y$

We will not provide the proof since this case is symmetric to the first case.

B PROOF OF THEOREM 1

Theorem 1. (copied) *Our Sigmoid \odot Tanh transformer is optimal (it minimizes the volume between the lower and upper plane) under the assumptions: (1) bounding planes are tangent to the curve at the respective anchor points, (2) bounding planes are parallel to either x or y axis. Planes computed using our transformer result in a volume strictly smaller than those computed using interval analysis.*

Proof. First note that $z_x^u, z_y^u, z_x^l, z_y^l$ are sound bounds by Appendix A. Assume z_x^u is chosen as the upper bound. W.l.o.g., suppose there exists another sound candidate upper bound ζ_x^u , satisfying (1) and (2), with smaller volume underneath it than z_x^u . Then ζ_x^u would have larger absolute slope on x than z_x^u . However, the slope of z_x^u is chosen as stiff as possible while remaining the soundness (Appendix A to see in detail). Hence, ζ_x^u would not be sound anymore with larger absolute coefficient. Contradict to the existence of sound ζ_x^u . Other cases can be proved with similar logic as well. \square

C VERIFICATION BY EXAMPLE

We assume the last sound frame $\mathbf{s}^{(t)}$ consists of two elements $s_1^{(t)}$ and $s_2^{(t)}$ such that: $s_1^{(t)} \in [0, 1]$ and $s_2^{(t)} \in [-2, -1]$. These constraints capture a noise perturbation of the sound and are depicted in the white box in the left part of Fig. 2. We describe analysis only at the last timestep t (the same process is repeated for every timestep).

We note that the DeepPoly abstraction (which we build on in this work) maintains four constraints for every element: a lower and upper constraints which are linear in terms of the previous elements as well as two interval constraints. This abstraction is exact for affine transformations, however, to handle non-linear operations, one has to create new abstract transformers. In our work we introduce such transformers and formally describe their operation in the next sections. In what follows, we show their effect on our running example. For the presentation below, our figure shows the linear constraints obtained by the verifier, but to avoid visual clutter, we do not show the two interval constraints (however, we do list them in the text).

Fast Fourier Transform The first operation in the audio processing stage is the Fast Fourier Transform (FFT) of the pre-emphasized input signal. It is a two-step process shown in dashed boxes in Fig. 2. The preemphasis is in fact an affine transform so we perform it jointly with the affine transform in the FFT. As the composition of two affine transforms is again affine, this

amounts to a single affine transform on the input. In our example, the composed affine transform is $y_1^{(t)} = s_1^{(t)} - s_2^{(t)}$ and $y_2^{(t)} = 2s_2^{(t)}$. Affine transforms can be captured exactly and here we obtain e.g., $s_1^{(t)} - s_2^{(t)} \leq y_1^{(t)} \leq s_1^{(t)} - s_2^{(t)}$. We also obtain the interval bounds $y_1^{(t)} \in [1, 3]$ and $y_2^{(t)} \in [-4, -2]$.

The next step in the computation of FFT is elementwise square of $\mathbf{y}^{(t)}$. We denote this operation as $\theta_1^{(t)} = (y_1^{(t)})^2$ and $\theta_2^{(t)} = (y_2^{(t)})^2$. The square operation is non-linear and cannot be captured exactly which means that we need to decide how to lose precision. Here, we apply our new square abstract transformer (formally defined in Section 4) which provides an optimal linear lower and upper bounds of the square function in terms of area. After applying this transformer, we obtain the bounds:

$$4y_1^{(t)} - 4 \leq \theta_1^{(t)} \leq 4y_1^{(t)} - 3 \quad -6y_2^{(t)} - 9 \leq \theta_2^{(t)} \leq -6y_2^{(t)} - 8$$

The interval bounds are calculated by:

$$\begin{aligned} \theta_1^{(t)} &\geq 4y_1^{(t)} - 4 = 4(s_1^{(t)} - s_2^{(t)}) - 4 \geq 4(0 - (-1)) - 4 = 0 \\ \theta_1^{(t)} &\leq 4y_1^{(t)} - 3 = 4(s_1^{(t)} - s_2^{(t)}) - 3 \leq 4(1 - (-2)) - 3 = 9 \\ \theta_2^{(t)} &\geq -6y_2^{(t)} - 9 = -6(2s_2^{(t)}) - 9 \geq -6(2 \cdot (-1)) - 9 = 3 \\ \theta_2^{(t)} &\leq -6y_2^{(t)} - 8 = -6(2s_2^{(t)}) - 8 \leq -6(2 \cdot (-2)) - 8 = 16 \end{aligned}$$

Hence, $\theta_1^{(t)} \in [0, 9]$ and $\theta_2^{(t)} \in [3, 16]$. Note those bounds are not exact but sound; even $y_1^{(t)} \in [1, 3]$ and $y_2^{(t)} \in [-4, -2]$, DAC calculates the concrete lower and upper bound with the expression to be consistent with other transformers, so the bounds might not be exact as $[1, 9]$ and $[4, 16]$. In practice, FFT is followed by another affine transform which adds together the real and complex component of each element, but we omit this for clarity as it is captured as before, without loss of precision.

Filterbanks Transform Our analysis continues with the computation of filter banks of the input, shown in solid boxes in Fig. 2. The first step is an affine transform and in our example we use: $\tilde{\psi}_1^{(t)} = 2\theta_1^{(t)} + \theta_2^{(t)}$ and $\tilde{\psi}_2^{(t)} = \theta_1^{(t)} + 3\theta_2^{(t)}$. Our abstraction is again exact here and additionally computes interval bounds $\tilde{\psi}_1^{(t)} \in [3, 34]$ and $\tilde{\psi}_2^{(t)} \in [9, 57]$. The final step in this transform is the elementwise logarithm of the input. We denote the operation as $\psi_1^{(t)} = \log(\tilde{\psi}_1^{(t)})$ and $\psi_2^{(t)} = \log(\tilde{\psi}_2^{(t)})$. As this is again a non-linear operation, we apply our new log transformer so to obtain:

$$\begin{aligned} 0.0783\tilde{\psi}_1^{(t)} + 0.8637 &\leq \psi_1^{(t)} \leq 0.0541\tilde{\psi}_1^{(t)} + 1.9178 \\ 0.0384\tilde{\psi}_2^{(t)} + 1.8511 &\leq \psi_2^{(t)} \leq 0.0303\tilde{\psi}_2^{(t)} + 2.4965 \end{aligned}$$

The interval bounds are calculated by:

$$\begin{aligned}
\psi_1^{(t)} &\geq 0.0783\tilde{\psi}_1^{(t)} + 0.8637 = 0.0783(2\theta_1^{(t)} + \theta_2^{(t)}) + 0.8637 \\
&\geq 0.0783(2(4y_1^{(t)} - 4) + (-6y_2^{(t)} - 9)) + 0.8637 \\
&= 0.0783(2(4(s_1^{(t)} - s_2^{(t)}) - 4) + (-6(2s_2^{(t)}) - 9)) + 0.8637 \\
&= 0.6264s_1^{(t)} - 1.566s_2^{(t)} - 0.4674 \geq 1.0986 \\
\psi_1^{(t)} &\leq 0.0541\tilde{\psi}_1^{(t)} + 1.9178 = 0.0541(2\theta_1^{(t)} + \theta_2^{(t)}) + 1.9178 \\
&\leq 0.0541(2(4y_1^{(t)} - 3) + (-6y_2^{(t)} - 8)) + 1.9178 \\
&= 0.0541(2(4(s_1^{(t)} - s_2^{(t)}) - 3) + (-6(2s_2^{(t)}) - 8)) + 1.9178 \\
&= 0.4328s_1^{(t)} - 1.082s_2^{(t)} + 1.1604 \leq 3.7572 \\
\psi_2^{(t)} &\geq 0.0384\tilde{\psi}_2^{(t)} + 1.8511 = 0.0384(\theta_1^{(t)} + 3\theta_2^{(t)}) + 1.8511 \\
&\geq 0.0384((4y_1^{(t)} - 4) + 3(-6y_2^{(t)} - 9)) + 1.8511 \\
&= 0.0384((4(s_1^{(t)} - s_2^{(t)}) - 4) + 3(-6(2s_2^{(t)}) - 9)) + 1.8511 \\
&= 0.1536s_1^{(t)} - 1.536s_2^{(t)} + 0.6607 \geq 2.1967 \\
\psi_2^{(t)} &\leq 0.0303\tilde{\psi}_2^{(t)} + 2.4965 = 0.0303(\theta_1^{(t)} + 3\theta_2^{(t)}) + 2.4965 \\
&\leq 0.0303((4y_1^{(t)} - 3) + 3(-6y_2^{(t)} - 8)) + 2.4965 \\
&= 0.0303((4(s_1^{(t)} - s_2^{(t)}) - 3) + 3(-6(2s_2^{(t)}) - 8)) + 2.4965 \\
&= 0.1212s_1^{(t)} - 1.212s_2^{(t)} + 1.6784 \leq 4.2236
\end{aligned}$$

In other words, $\psi_1^{(t)} \in [1.0986, 3.7572]$ and $\psi_2^{(t)} \in [2.1967, 4.2236]$. Again, these bounds are sound since $[\log 3, \log 34] \subset [1.0986, 3.7572]$, $[\log 9, \log 57] \subset [2.1967, 4.2236]$.

Discrete Cosine Transform and ReLU After the Filterbanks Transform, the input is passed through the Discrete Cosine Transform (DCT) followed by a Lifting operation. The analysis result of these steps is then provided as an input to a fully connected (FC) layer followed by a ReLU activation. To ease presentation, in our example we combine DCT, Lifting and FC layer in a single affine transform: $\tilde{x}_1^{(t)} = \psi_1^{(t)} - \psi_2^{(t)} + 4$ and $\tilde{x}_2^{(t)} = 4\psi_1^{(t)} - \psi_2^{(t)}$. We show this transform in a dotted box in Fig. 2. This is again captured exactly in our abstraction along with interval bounds $\tilde{x}_1^{(t)} \in [0.875, 5.5605]$, $\tilde{x}_2^{(t)} \in [0.1708, 12.8321]$. The affine transform is followed by a ReLU activation $x_1^{(t)} = \max(0, \tilde{x}_1^{(t)})$, $x_2^{(t)} = \max(0, \tilde{x}_2^{(t)})$. In general, we use the ReLU transformer defined in Singh et al. (2019a), which for this example produces: $x_1^{(t)} = \tilde{x}_1^{(t)}$ and $x_2^{(t)} = \tilde{x}_2^{(t)}$.

LSTM analysis After the verifier completes the audio processing stage, its output is passed as input to the LSTM cell. This cell also receives a hidden state and a cell state from the previous timestep (shown as a blue box in Fig. 2). In our example, we assume these are given as: $h_1^{(t-1)}, h_2^{(t-1)}, c_1^{(t-1)}, c_2^{(t-1)} \in [0.9, 1]$. We note that these elements usually have different interval bounds, but for simplicity in our example we use the same intervals. We focus on the first neuron in the LSTM and compute pre-activations in our example for the forget gate $f_1^{(t)} = x_1^{(t)}/4$, input gate $i_1^{(t)} = 2h_2^{(t-1)}$, output gate $o_1^{(t)} = h_1^{(t-1)}$ and cell state $\tilde{c}^{(t)} = h_1^{(t-1)} - x_2^{(t)}/4$.

In order to update the cell state, we need to compute: $c_1^{(t)} = \sigma(f_1^{(t)}) \cdot c_1^{(t-1)} + \sigma(i_1^{(t)}) \cdot \tanh(\tilde{c}_1^{(t)})$. The left and right summands are computed using our new binary abstract transformers for $\sigma(x) \cdot y$ and $\sigma(x) \cdot \tanh(y)$ expressions, respectively. Applying our abstract transformers on the summands produces the following bounds:

$$\begin{aligned}
0.1891f_1^{(t)} + 0.4576 &\leq \sigma(f_1^{(t)}) \cdot c_1^{(t-1)} \leq 0.1596f_1^{(t)} + 0.5787 \\
0.0341\tilde{c}_1^{(t)} - 0.7847 &\leq \sigma(i_1^{(t)}) \cdot \tanh(\tilde{c}_1^{(t)}) \leq 0.3945\tilde{c}_1^{(t)} + 0.2769
\end{aligned}$$

Summing up the above inequalities grants the upper and lower bounds of $c_1^{(t)}$ in terms of $\mathbf{x}^{(t)}$, $\mathbf{h}^{(t-1)}$, and $\mathbf{c}^{(t-1)}$:

$$\begin{aligned} c_1^{(t)} &\geq 0.1891f_1^{(t)} + 0.0341\tilde{c}_1^{(t)} - 0.3271 \\ &= 0.1891(x_1^{(t)}/4) + 0.0341(h_1^{(t-1)} - x_2^{(t)}/4) - 0.3271 \\ &\geq -0.3644 \\ c_1^{(t)} &\leq 0.1596f_1^{(t)} + 0.3945\tilde{c}_1^{(t)} + 0.8556 \\ &= 0.1596(x_1^{(t)}/4) + 0.3945(h_1^{(t-1)} - x_2^{(t)}/4) + 0.8556 \\ &\leq 1.4551 \end{aligned}$$

and get $c_1^{(t)} \in [-0.3644, 1.4551]$. We omit the back-substitution steps since we do not lose precision over the affine transformations from $\mathbf{x}^{(t)}$, and note that this calculation is based on the assumption that the bounds of $\mathbf{h}^{(t)}$ and $\mathbf{c}^{(t-1)}$ are given constant. In practice, we recursively apply the process for those vectors to express the bounds in terms of $\mathbf{x}^{(t)}$, $\mathbf{x}^{(t-1)}$, \dots .

The next hidden state is computed as $h_1^{(t)} = \sigma(o_1^{(t)}) \cdot \tanh(c_1^{(t)})$. We apply our abstract transformer for the $\sigma(x) \cdot \tanh(y)$ expression, we obtain:

$$\begin{aligned} h_1^{(t)} &\geq 0.4906c_1^{(t)} - 0.0764 \\ &\geq 0.4906(0.1891f_1^{(t)} + 0.0341\tilde{c}_1^{(t)} - 0.3271) - 0.0764 \\ &\geq -0.2551 \\ h_1^{(t)} &\leq 0.1433c_1^{(t)} + 0.4471 \\ &\leq 0.1433(0.1596f_1^{(t)} + 0.3945\tilde{c}_1^{(t)} + 0.8556) + 0.4471 \\ &\leq 0.6556 \end{aligned}$$

i.e., $h_1^{(t)} \in [-0.2551, 0.6556]$. An analogous computation is performed for $h_2^{(t)}$. In this example we will assume $h_2^{(t)} = 0$ concretely.

Robustness certification using DeepPoly The hidden states in the LSTM at the final timestep are passed through a fully connected layer without activation. In our example we assume that logits after the layer are obtained with the following formula: $l_1 = h_1^{(t)} + 0.24$ and $l_2 = h_2^{(t)}$. These are shown in the final box of Fig. 2. To certify that the neural network classifies the input to class 1, we need to prove that $l_1 - l_2 > 0$. We now apply the same back-substitution technique as Singh et al. (2019a):

$$\begin{aligned} l_1 - l_2 &= h_1^{(t)} - h_2^{(t)} + 0.24 \\ &\geq 0.4906(0.1891f_1^{(t)} + 0.0341\tilde{c}_1^{(t)} - 0.3271) - 0.0764 + 0.24 \\ &= 0.0927f_1^{(f)} + 0.0167\tilde{c}_1^{(t)} + 0.0031 \\ &= 0.0927(x_1^{(t)}/4) + 0.0167(h_1^{(t-1)} - x_2^{(t)}/4) + 0.0031 \\ &\stackrel{\text{(applying concrete bound to } h_1^{(t-1)} \text{ for demonstration)}}{\geq} 0.0231x_1^{(t)} - 0.0042x_2^{(t)} + 0.0181 \\ &= 0.0231(\psi_1^{(t)} - \psi_2^{(t)} + 4) - 0.0042(4\psi_1^{(t)} - \psi_2^{(t)}) + 0.0181 \\ &= 0.0063\psi_1^{(t)} - 0.0189\psi_2^{(t)} + 0.1105 \\ &\stackrel{\text{halt the computation and plug in the bounds}}{\geq} 0.0063 \cdot 1.0986 - 0.0189 \cdot 4.2236 + 0.1105 \\ &\geq 0.0375 \end{aligned}$$

For the purpose of demonstration, we stop here and plug in previously obtained interval bounds for $\psi^{(t)}$. As this value is greater than 0, robustness is established.

D MATHEMATICAL DERIVATION OF LSTM TRANSFORMER

LSTM cell receives not only the resulting neurons from the pre-processing stage but a hidden state and a cell state from the previous timestep. To incorporate with all those incoming values, we extend

the scope of the LSTM equations defined in Section 2. Let d be the dimension of the input and h be the dimension of states of the cell. To standardize the operations performed within the LSTM cell, we append $\mathbf{0}_{d \times d} = [0]_{d \times d}$ and $\mathbf{0}_d = [0]_d$ below to each kernel and bias respectively to express the formula as

$$\begin{aligned} \mathbf{f}_0^{(t)} &= [\mathbf{x}^{(t)}, \mathbf{h}^{(t-1)}, \mathbf{c}^{(t-1)}] \mathbf{W}'_f + \mathbf{b}'_f & \mathbf{o}_0^{(t)} &= [\mathbf{x}^{(t)}, \mathbf{h}^{(t-1)}, \mathbf{c}^{(t-1)}] \mathbf{W}'_o + \mathbf{b}'_o \\ \mathbf{i}_0^{(t)} &= [\mathbf{x}^{(t)}, \mathbf{h}^{(t-1)}, \mathbf{c}^{(t-1)}] \mathbf{W}'_i + \mathbf{b}'_i & \tilde{\mathbf{c}}_0^{(t)} &= [\mathbf{x}^{(t)}, \mathbf{h}^{(t-1)}, \mathbf{c}^{(t-1)}] \mathbf{W}'_{\tilde{c}} + \mathbf{b}'_{\tilde{c}} \end{aligned} \quad (1)$$

Then the cell state and hidden state computations can be rewritten as

$$\begin{aligned} \mathbf{c}^{(t)} &= \sigma(\mathbf{f}_0^{(t)}) \odot \mathbf{c}^{(t-1)} + \sigma(\mathbf{i}_0^{(t)}) \odot \tanh(\tilde{\mathbf{c}}_0^{(t)}) \\ &= \sigma([\mathbf{x}^{(t)}, \mathbf{h}^{(t-1)}, \mathbf{c}^{(t-1)}] \mathbf{W}'_f + \mathbf{b}'_f) \odot ([\mathbf{x}^{(t)}, \mathbf{h}^{(t-1)}, \mathbf{c}^{(t-1)}] [\mathbf{0}_{h \times (d+h)}, \mathbf{I}_h]^T) \\ &\quad + \sigma([\mathbf{x}^{(t)}, \mathbf{h}^{(t-1)}, \mathbf{c}^{(t-1)}] \mathbf{W}'_i + \mathbf{b}'_i) \odot \tanh([\mathbf{x}^{(t)}, \mathbf{h}^{(t-1)}, \mathbf{c}^{(t-1)}] \mathbf{W}'_{\tilde{c}} + \mathbf{b}'_{\tilde{c}}) \end{aligned} \quad (2)$$

$$\begin{aligned} \mathbf{h}^{(t)} &= \sigma(\mathbf{o}_0^{(t)}) \odot \tanh(\mathbf{c}^{(t)}) \\ &= \sigma([\mathbf{x}^{(t)}, \mathbf{h}^{(t-1)}, \mathbf{c}^{(t-1)}] \mathbf{W}'_o + \mathbf{b}'_o) \odot \tanh(\mathbf{c}^{(t)}) \end{aligned} \quad (3)$$

As is described in detail in Section 5, $f(x, y) = \sigma(x) \cdot \tanh(y)$ and $g(x, y) = \sigma(x) \cdot y$ can be bounded with two planes regarding the operands' lower and upper bounds. In other words, for any given two real values, $x, y \in \mathbb{R}$, $x \in [l_x, u_x]$, $y \in [l_y, u_y]$, our finding guarantees the planar bounds of f and g with the coefficients built by linear combination of l_x, u_x, l_y, u_y . For a single neuron $c_j^{(t)}$ in $\mathbf{c}^{(t)}$, the upper bound can be expressed from Eq. (2):

$$\begin{aligned} c_j^{(t)} &= \sigma([\mathbf{x}^{(t)}, \mathbf{h}^{(t-1)}, \mathbf{c}^{(t-1)}] [\mathbf{W}'_f]_{:,j} + [\mathbf{b}'_f]_j) \cdot ([\mathbf{x}^{(t)}, \mathbf{h}^{(t-1)}, \mathbf{c}^{(t-1)}] [\mathbf{0}_{d+h}, [\mathbf{I}_h]_{j,:}]^T) \\ &\quad + \sigma([\mathbf{x}^{(t)}, \mathbf{h}^{(t-1)}, \mathbf{c}^{(t-1)}] [\mathbf{W}'_i]_{:,j} + [\mathbf{b}'_i]_j) \cdot \tanh([\mathbf{x}^{(t)}, \mathbf{h}^{(t-1)}, \mathbf{c}^{(t-1)}] [\mathbf{W}'_{\tilde{c}}]_{:,j} + [\mathbf{b}'_{\tilde{c}}]_j) \\ &\leq A_u([\mathbf{x}^{(t)}, \mathbf{h}^{(t-1)}, \mathbf{c}^{(t-1)}] [\mathbf{W}'_f]_{:,j} + [\mathbf{b}'_f]_j) + B_u([\mathbf{x}^{(t)}, \mathbf{h}^{(t-1)}, \mathbf{c}^{(t-1)}] [\mathbf{0}_{d+h}, [\mathbf{I}_h]_{j,:}]^T) + C_u \\ &\quad + D_u([\mathbf{x}^{(t)}, \mathbf{h}^{(t-1)}, \mathbf{c}^{(t-1)}] [\mathbf{W}'_i]_{:,j} + [\mathbf{b}'_i]_j) + E_u([\mathbf{x}^{(t)}, \mathbf{h}^{(t-1)}, \mathbf{c}^{(t-1)}] [\mathbf{W}'_{\tilde{c}}]_{:,j} + [\mathbf{b}'_{\tilde{c}}]_j) + F_u \\ &= \mathbf{x}^{(t)} \mathbf{w}_x + \mathbf{h}^{(t-1)} \mathbf{w}_h + \mathbf{c}^{(t-1)} \mathbf{w}_c + b \end{aligned} \quad (4)$$

where A_u, \dots, F_u are calculated real values by Section 5, and \mathbf{w} and b are the simplified linear coefficients of each vector and bias term, respectively. We also can get the upper bound of $h_j^{(t)}$ by plugging Eq. (4) in Eq. (3), and similarly for the lower bounds of those states.

Note these linear bounds makes possible to recursively apply this step to get desired bounds, and can be branched in any depth for the trade-off between the precision and the complexity.